Paper Number: IWSH2025-082

The 13th International Workshop on Ship and Marine Hydrodynamics
Fukuoka, Japan, August 25 - 28, 2025

Phase-Resolved Wave Prediction using Ship Motion Measurements

Malwin Wermbter, Johanna Serr, and Moustafa Abdel-Maksoud

Institute for Fluid Dynamics and Ship Theory, Hamburg University of Technology, Hamburg, Germany
Corresponding author: malwin.wermbter@tuhh.de

Abstract. The study focuses on the potential of wave prediction and forecasting during operations involving multiple ships of varying sizes. By combining phase-resolved wave estimation with phase-resolved wave prediction to a ship located leeward of another ship, the approach aims to reduce the risk during critical operations by forecasting the wave profile. Wave profile estimations are obtained using Prolate Spheroidal Wave Functions (PSWF) from ship motion measurements. The predicted wave profiles from multiple points along the ship are combined in a linear phase-resolved wave prediction. The wave prediction for the leeward ship is calculated using linear wave theory (LWT). The motion behavior of a barge, and a down scaled version of it, called "small barge", is investigated numerically. The results demonstrate that PSWF estimation can be employed to reconstruct the wave profile along the barges. The results indicate that the estimation and prediction are accurate in short-crested seaways. Three case studies confirm that high motions amplitudes and the size of the forward ship dictate the prediction accuracy for the combined methodology.

Keywords: Phase-resolved wave prediction, Motion measurements, Prolate spheroidal wave functions, Forward speed, Short-crested seaway

1 Introduction

Operations at sea are significantly influenced by wave conditions, which can limit operational capabilities. Phase-resolved wave prediction allows to calculate wave amplitudes as well as their phase information in order to reconstruct the wave profile in time and space. The knowledge of the wave profile allows to assess the risk of an operation or even actively control of the motion, e.g. with fins or roll damping tanks. For operations, which can not be postponed due to the weather such as the recovery of dinghies, phase-resolved waves enable to identify time windows with low wave amplitudes, so called quiescent periods [1]. The aim of this study is to establish an algorithm solely based on motion measurements and estimate waves at one or multiple ships and apply a wave prediction technique to translate these measurements to a ship downstream. Mounet et al. [12] took a similar approach for estimation of spectral parameters with the wave buoy analogy showing that the combined information of multiple ships increase the accuracy of the estimations.

Phase-resolved wave prediction is split into two steps: The assimilation of wave components at one or more measurement pointa and the prediction at the downstream estimation point [7]. A cost-effective option for wave assimilation onboard of ships is motion-based wave estimation. Takami et al. [18] point out that accurately estimating phase components in a short time window using the commonly employed fast Fourier transform (FFT) is challenging due to the frequency resolution. Other estimation techniques, based on the Kalman filter, have shown success in reconstructing wave profiles in long-crested waves [5][8]. Although, the Kalman filter requires a calibration phase [18], which may affect its accuracy in varying wave conditions. Prolate spheroidal wave functions (PSWF) are introduced by Takami et al [15][16][17][18] to ship wave estimation. PSWF enable to reconstruct the motion in short time windows with a finer frequency resolution than the FFT. The incorporation of the motion transfer function enables to reconstruct the wave encounter angles, spectral parameters, ship roll damping and the wave profile along the ship. In comparison to the Kalman filter, PSWF require less input and no calibration phase, however the accuracy of the transfer function has to be accurate.

Predicting waves at a downstream point requires the knowledge of wave amplitudes, phases and directions at all relevant wave frequencies. Cademartori et al. [1] reviewed existing phase-resolved prediction methods

and classified them as physical, hybrid and data-driven models. They concluded that hybrid methodologies seem to be most promising, since they combine the strengths of various approaches, particularly in reconstructing nonlinear phenomena while maintaining computational efficiency. This study focuses on wave prediction techniques that are faster than real time in order to forecast the motion of the second ship. The use of wave profiles from the PSWF estimation already limits the accuracy to linear phenomena due to the use of the linear transfer function. Data-driven methods, such as artificial intelligence (AI) methods, have shown potential for improving prediction accuracy. Chen et al. [2] state that the use of an artificial neural network increases the prediction horizon and is beneficial in determining wave conditions with large spreading angles. Compared to identification methods using an equation system to identify the wave components [3][7], data-driven methods require a large amount of realistic training data. A recent hybrid method by Liu et al. [10] incorporates linear wave theory (LWT) prediction into a physics informed neural network, which outperforms the LWT prediction. The main advantage of using LWT is its simplicity, computation speed and the acceptable accuracy within the predictable zone [14].

This study combines the PSWF method for wave profile estimation by Takami et al. [18] with the phase-resolved wave prediction in short crested seaways. The assimilation of PSWF predictions is done according to the algorithm for LWT by Kim et al. [7], as the estimated wave profiles by PSWF are also linear. The wave profile is estimated at multiple positions along the ships and used in the assimilation process. The remainder of this study is organized as follows. In Section 2 the methods are defined, split into the wave estimation and the wave prediction. Section 3 shows the geometrical properties of the investigated barge and details of the numerical data generation. Section 4 presents results verifiying the individual methods and case studies verifying the combined methodology.

2 Methodology

2.1 Wave profile estimation using PSWF

The wave profile estimation at a ship is calculated using the PSWF method proposed by Takami et al. [18]. The required input is a time window size T of arbitrary motion measurements. Increasing the number of degrees of freedom (DOF) increases the information available during parameter estimation, but also increases the computational effort.

PSWF enable the reconstruction of the ship motions r for each DOF k by identifying the phase components u and $\bar{u}$. The phase components are calculated for several frequencies, constrained by an input frequency Ω, above which reconstruction is not possible. The response spectra S used for motion reconstruction is calculated from the Fourier transform of the time series

$$r_{\mathrm{k}}(t) \approx \sum_{\mathrm{i}=1}^{N_\omega} \sqrt{S_{\mathrm{k}}(\omega_{\mathrm{i}})\,\mathrm{d}\omega}\,(u_{\mathrm{i,k}}\cos(\omega_{\mathrm{i}}t) - \bar{u}_{\mathrm{i,k}}\sin(\omega_{\mathrm{i}}t))\ . \tag{1}$$

The number of frequencies N_ω is a function of the time window size T and the maximal frequency Ω, for details see Takami et al. [18]. The phase angles φ of the transfer functions of varying DOF are subtracted and added into Eq. (1). It is possible to reconstruct the motion of DOF k with the phase components of DOF l

$$\begin{aligned} r_{\mathrm{k}}^{\phi}(t) \approx \sum_{\mathrm{i}=1}^{N_\omega} \sum_{\mathrm{l}=1,\mathrm{l}\neq\mathrm{k}}^{N_{\mathrm{DOF}}} \sqrt{S_{\mathrm{k}}(\omega_{\mathrm{i}})\,\mathrm{d}\omega}(u_{\mathrm{i,l}}\cos(\omega_{\mathrm{i}}t - \varphi_{\mathrm{l}}(\omega_{\mathrm{i}},\phi) + \varphi_{\mathrm{k}}(\omega_{\mathrm{i}},\phi)) \\ - \bar{u}_{\mathrm{i,l}}\sin(\omega_{\mathrm{i}}t - \varphi_{\mathrm{l}}(\omega_{\mathrm{i}},\phi) + \varphi_{\mathrm{k}}(\omega_{\mathrm{i}},\phi)))\,. \end{aligned} \tag{2}$$

The manipulation is calculated for each unique DOF combination and summed for all DOF m. The correlation ρ between two time series r_{a} and r_{b} quantifies their similarity

$$\rho = \frac{\mathrm{cov}(r_{\mathrm{a}}, r_{\mathrm{b}})}{\sigma(r_{\mathrm{a}})\sigma(r_{\mathrm{b}})}\,. \tag{3}$$

A correlation of 1 indicates identical motions, while -1 represents anti-proportional motions. The correlation is calculated for each encounter angle ϕ_{e} in relation to the original time series. The encounter angle maximizing

the correlation is selected and its RAO $\hat{Y}(\phi_\mathrm{e})$ is used for further computations. The phase components and encounter angle estimation deliver all necessary information for the phase-resolved estimation of the wave profile

$$\zeta(t) \approx \sum_{\mathrm{i}=1}^{N_\omega} \frac{\sum_{\mathrm{k}=1}^{N_\mathrm{DOF}} \frac{\sqrt{S_\mathrm{k}(\omega_\mathrm{i})\mathrm{d}\omega}|\hat{Y}_{\mathrm{p,k}}(\omega_\mathrm{i},\phi_\mathrm{e})|(u_{\mathrm{i,k}}\cos(\omega_\mathrm{i}t+\varphi_\mathrm{k}(\omega_\mathrm{i},\phi_\mathrm{e}))-\bar{u}_{\mathrm{i,k}}\sin(\omega_\mathrm{i}t+\varphi_\mathrm{k}(\omega_\mathrm{i},\phi_\mathrm{e})))}{|\hat{Y}^2_{\mathrm{p,k,max}}|}}{\sum_{\mathrm{k}=1}^{N_\mathrm{DOF}}\left(\frac{|\hat{Y}_{\mathrm{p,k}}(\omega_\mathrm{i},\phi_\mathrm{e})|}{|\hat{Y}_{\mathrm{p,k,max}}|}\right)^2}\,. \tag{4}$$

To avoid numerical instabilities with small amplitudes, the wave profile is normalized with the maximal amplitude $|\hat{Y}_{\mathrm{p,k,max}}|$. The calculation is limited to amplitudes greater than $\frac{|\hat{Y}_{\mathrm{p,k}}(\omega)|}{|\hat{Y}_{\mathrm{p,k,max}}|} > 0.1$.

The wave profile estimation and encounter angle estimation can be performed for arbitrary points p along the ship. The motions at these points can be obtained from additional motion measurements or under assumption of a rigid body and application of relative kinematics [4]. The transfer functions are linear and can also be transformed to a point with coordinate vector $(x_\mathrm{p}, y_\mathrm{p}, z_\mathrm{p})^T$ using relative kinematic relations [11].

Equation (4) has to be adapted, since the resulting wave profile $\zeta(t)$ is valid at the centre of gravity. The wave profile at a point p results from multiplying the wave at the center of gravity $\zeta(\omega_{\mathrm{e,i}}, \phi_\mathrm{j}, t)$ with the phase shift due to the location of the point

$$\zeta_\mathrm{p}(t) = \sum_{i=1}^{N_\omega}\sum_{j=1}^{N_\phi} \mathrm{Re}\left(\zeta(\omega_{\mathrm{e,i}}, \phi_\mathrm{j}, t)\cdot e^{i(-k_\mathrm{i}x_\mathrm{p}\cos(\phi_\mathrm{j})+k_\mathrm{i}y_\mathrm{p}\sin(\phi_\mathrm{j}))}\right)\,. \tag{5}$$

Equation (4) is valid for the wave profile ζ_p if the transfer function is multiplied with the phase shift of the waves at point p

$$\hat{Y}_{\mathrm{pp,k}}(\omega_\mathrm{i}, \phi_\mathrm{j}) = \hat{Y}_{\mathrm{p,k}}(\omega_\mathrm{i}, \phi_\mathrm{j})\cdot e^{-i(-k_\mathrm{i}x_\mathrm{p}\cos(\phi_\mathrm{j})+k_\mathrm{i}y_\mathrm{p}\sin(\phi_\mathrm{j}))}\,. \tag{6}$$

2.2 Predictable zone and wave prediction using LWT

The following section presents the formulae to generate a phase-resolved prediction based on measurements from a ship a to a ship b. The wave prediction procedure is divided into two steps: defining the predictable zone and performing the prediction itself. The predictable zone is derived from the theory of Qi et al. [14]. The predictable zone is defined as the time window where according to linear wave theory a prediction should be possible. The zone is constrained by the slowest and fastest wave group speeds. Qi et al. [14] defines the time window for moving observation points in a short-crested seaway as $\mathit{\Pi} \in [T_0, T_1]$ with the start time T_0 and end time T_1. The time window is the union of each point $\boldsymbol{x}_\mathrm{p}$, but the intersection of each frequency and direction

$$\mathit{\Pi}(t) = \bigcap_{\mathrm{i}=1}^{N_\omega}\bigcap_{\mathrm{j}=1}^{N_\phi}\bigcup_{\mathrm{p}=1}^{N_\mathrm{x}} \mathit{\Pi}(\omega_\mathrm{i}, \phi_\mathrm{j}, \boldsymbol{x}_\mathrm{p}, t)\,. \tag{7}$$

In the one-dimensional case, the predictable zone starts when the slowest component arrives at b and ends when the fastest wave arrives at point b after the time window T ended. Equation (7) indicates that increasing the number of points may increase the predictable zone at b. Although, a highly spread seaway reduces the predictable time window compared to a long-crested seaway.

Fig. 1 shows two ships with their heading angles ψ and the wave direction ϕ. The distance d is always measured along the wave direction and the global coordinate system (x, y) is used throughout the following calculations to discretize equation (7). For each frequency and direction, the encountered wave speed at ship b is given by the sum of the ship speed v_b and the group speed c_gr

$$c_\mathrm{e} = c_\mathrm{gr} + v_\mathrm{b}\cos(\phi + \psi_\mathrm{b} - 180°)\,. \tag{8}$$

Measuring the distance along the wave direction is beneficial when using both heading angles and wave directions, but may result in the distance being zero if x-coordinates are used. These cases are replaced by calculating the coefficients α with y-coordinates. The start time is calculated by solving the equation T_0 and

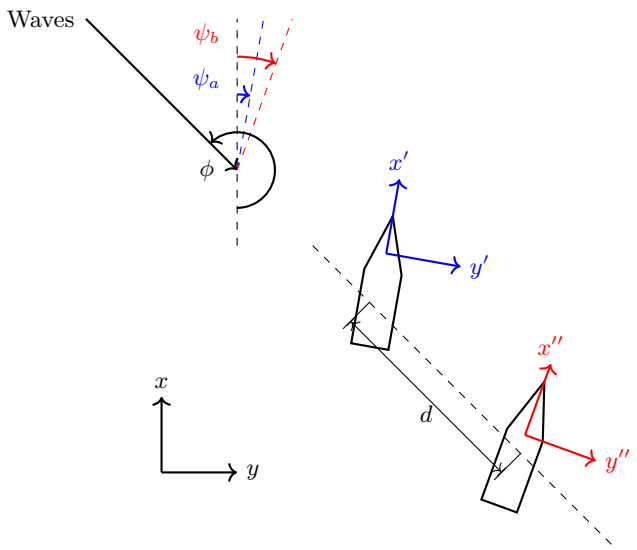

Fig. 1: Definition of global coordinate system (x, y) for wave prediction between two ships a and b with varying heading angles ψ and waves from direction ϕ.

the end time T_1

$$T_0 = \frac{d(t)}{c_\mathrm{e}} = \frac{\alpha_0}{\alpha_2 - \alpha_1}\,, \tag{9}$$

$$T_1 = T + \frac{d(t)}{c_\mathrm{e}} = \frac{\alpha_0 + \alpha_2 T}{\alpha_2 - \alpha_1}\,. \tag{10}$$

The coefficients follow from

$$\alpha_0 = \begin{cases} x_{\mathrm{b},0} - x_{\mathrm{a},0} \\ y_{\mathrm{b},0} - y_{\mathrm{a},0} \end{cases} \quad \alpha_1 = \begin{cases} v_\mathrm{b}\cos\psi_\mathrm{b} - v_\mathrm{a}\cos\psi_\mathrm{a} \\ v_\mathrm{b}\sin\psi_\mathrm{b} - v_\mathrm{a}\sin\psi_\mathrm{a} \end{cases} \quad \alpha_2 = \begin{cases} \frac{c_\mathrm{gr} + v_\mathrm{b}\cos(\phi+\psi_\mathrm{b}-180^\circ)}{\cos\phi} & \cos\phi \neq 0 \\ -\frac{c_\mathrm{gr} + v_\mathrm{b}\cos(\phi+\psi_\mathrm{b}-180^\circ)}{\sin\phi} & \text{otherwise} \end{cases}. \tag{11}$$

The considered frequency range is limited between the frequency corresponding to $c_{\mathrm{gr,max}}$ and that of $c_{\mathrm{gr,min}}$, ensuring that 85% of the total energy is captured within the spectrum [9]. Ship motion measurements combined with wave estimation using PSWF, yield a wave spectrum dependent on the encounter frequency. The required group velocities are obtained by transforming to absolute frequencies, following the approach established by Nielsen [13]. The directions are distributed in the interval $[\phi - 45^\circ, \phi + 45^\circ]$ around the main wave direction.

Knowledge of the predictable zone and the estimated wave profiles is required for the data assimilation and prediction of waves to ship b. This study employs the phase-resolved wave prediction for linear wave theory by Kim et al. [6]. The procedure is split into the assimilation and prediction. The assimilation solves a linear equation system for the phase components v and $\bar{v}$, which are used to reconstruct the elevation ζ at an observation point a

$$\zeta_\mathrm{a}(\boldsymbol{x}_\mathrm{j}, t_\mathrm{j}) = \sum_{\mathrm{i}=1}^{N_\omega \cdot N_\phi} v_\mathrm{i}\cos f_{\mathrm{i,j}} + \bar{v}_\mathrm{i}\sin f_{\mathrm{i,j}}\,. \tag{12}$$

Wave frequencies and directions are written into a single vector for simplicity. The phase component factor f is dependent on the encounter frequency, time and position

$$f_{\mathrm{i,j}} = \omega_{\mathrm{e,i}} t_\mathrm{j} - k_\mathrm{i}(x_{\mathrm{r,j}}\cos\phi_\mathrm{i} - y_{\mathrm{r,j}}\sin\phi_\mathrm{i})\,. \tag{13}$$

The position used for reconstruction is the relative vector from the prediction point to the observation point $\boldsymbol{x}_\mathrm{r} = \boldsymbol{x}_\mathrm{a} - \boldsymbol{x}_\mathrm{b}$. The equation system is set up for each time window individually

$$\begin{bmatrix} \left[\sum_{\mathrm{n}=1}^{N} \cos f_{\mathrm{i,n}} \cos f_{\mathrm{j,n}}\right]_{\mathrm{N}\times\mathrm{N}} & \left[\sum_{\mathrm{n}=1}^{N} \sin f_{\mathrm{i,n}} \cos f_{\mathrm{j,n}}\right]_{\mathrm{N}\times\mathrm{N}} \\ \left[\sum_{\mathrm{n}=1}^{N} \cos f_{\mathrm{i,n}} \sin f_{\mathrm{j,n}}\right]_{\mathrm{N}\times\mathrm{N}} & \left[\sum_{\mathrm{n}=1}^{N} \sin f_{\mathrm{i,n}} \sin f_{\mathrm{j,n}}\right]_{\mathrm{N}\times\mathrm{N}} \end{bmatrix} \cdot \begin{bmatrix} v_0 \\ \dots \\ \bar{v}_0 \\ \dots \end{bmatrix} = \begin{bmatrix} \left[\sum_{\mathrm{n}=1}^{N} \zeta_{\mathrm{a,n}} \cos f_{\mathrm{i,n}}\right]_{\mathrm{N}\times1} \\ \left[\sum_{\mathrm{n}=1}^{N} \zeta_{\mathrm{a,n}} \sin f_{\mathrm{i,n}}\right]_{\mathrm{N}\times1} \end{bmatrix} . \tag{14}$$

The wave prediction is calculated without an additional positional vector in the phase components

$$\zeta_\mathrm{b}(t) = \sum_{\mathrm{i}=1}^{N} v_\mathrm{i} \cos(\omega_{\mathrm{e,i}} t) + \bar{v}_\mathrm{i} \sin(\omega_{\mathrm{e,i}} t) \,. \tag{15}$$

We applied the prediction to the same 60 s time window as used for the PSWF estimates. If the predictable zone is not continuous in time with the previous one, the time window size is iteratively increased until T_0 is smaller than the end time of the previous prediction. A wave forecast at ship b is feasible within the interval $[T, T_1]$, if the end time of the predictable zone exceeds the time window size.

3 Numerical data generation

Numerical wave profiles were generated using a JONSWAP spectrum with 30 frequencies and 5 wave directions. The wave heights and periods were varied and the resulting wave amplitudes were analyzed accordingly. The time series were generated for each ship and motion point

$$\zeta_\mathrm{e}(t) = \sum_{i=1}^{N_\omega} \sum_{j=1}^{N_\phi} \mathrm{Re}\left(\zeta(\omega_{\mathrm{e,i}}, \phi_\mathrm{j}) e^{i(\omega_{\mathrm{e,i}} t - k_\mathrm{i}(x_\mathrm{p}+x_0)\cos(\phi_\mathrm{j}) + k_\mathrm{i}(y_\mathrm{p}+y_0)\sin(\phi_\mathrm{j}) + \varphi_{\mathrm{i,j}})}\right) . \tag{16}$$

Subscript e denotes the encountered wave elevation at a motion point. Position $(x_\mathrm{p}, y_\mathrm{p})^T$ defines the location of the motion point, while (x_0, y_0) represents the ship's initial position in global coordinates. The motions were calculated by inserting the RAO $\hat{Y}$ of the specific DOF and motion point

$$r_{\mathrm{p,k}}(t) = \sum_{i=1}^{N_\omega} \sum_{j=1}^{N_\phi} \mathrm{Re}\left(\hat{Y}_{\mathrm{p,k}}(\omega_{\mathrm{e,i}}, \phi_\mathrm{j}) \zeta(\omega_{\mathrm{e,i}}, \phi_\mathrm{j}) e^{i(\omega_{\mathrm{e,i}} t - k_\mathrm{i} x_0 \cos(\phi_\mathrm{j}) + k_\mathrm{i} y_0 \sin(\phi_\mathrm{j}) + \varphi_{\mathrm{i,j}})}\right) . \tag{17}$$

Since the RAO calculation already accounts for the motion point coordinates, they are not explicitly required in the motion computation.

Table 1: Dimensions of the barge in full scale (barge) as well as the scaled barge (small barge)

Property		Unit	Barge	Small Barge
Length	L	[m]	122	19.4
Breadth	B	[m]	32.2	5.12
Draught	D	[m]	5.16	0.82
Froude number	Fn	[-]	0.058	0.145
Speed	v	[m/s]	2	2

Evaluations were conducted for a barge with a length of 122 m. To verify the combined estimation and prediction, three case studies were performed. The case studies consist of the barge and scale barged, referred to as the "small barge". Tab. 1 lists the geometrical parameters of the barge and the small barge. In all case studies, the barges proceed at the same speed and heading. The case studies cover 3 scenarios:

1. The small barge operates in front of the barge
2. The barge operates in front of the small barge
3. Two small barges operate in front of the barge with a lateral distance of y=40 m

Each case study was evaluated over a spatial domain of 150 m × 150 m, measured from the stern of the leading vessel in case study 1 and 2, and from the midpoint between the two small barges in case 3.

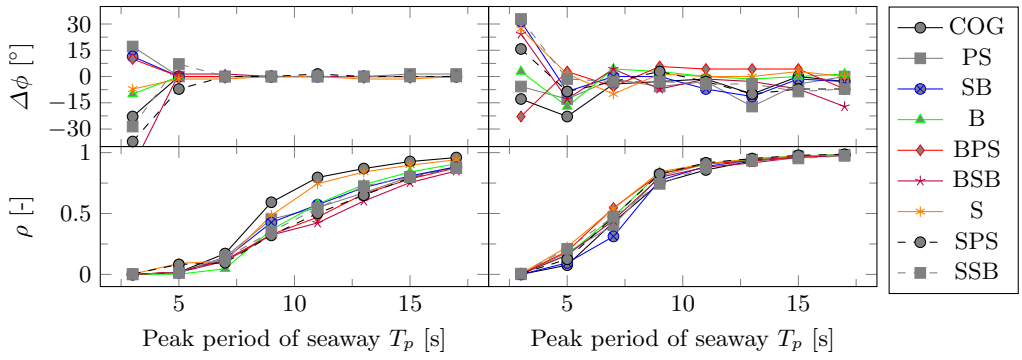

(a) Barge (b) Small Barge

Fig. 2: Comparison of mean difference from numerical input data for angle and correlation for various motion points along the ships. The left column shows results for the barge and the right column for the small barge. Results are averaged for encounter angles from 0° to 180° in 30° steps. (COG) indicates the motion point situated at the center of gravity. Additional points are at starboard (SB), portside (PS), stern (S) and bow (B) as well as combinations of the previous points.

4 Results and Discussion

Results are split into verification of the wave estimation and the verification of wave prediction with the numerical data sets from section 3. Afterwards the results of the three case studies are presented to verify the combined methodology.

4.1 Verification of wave estimation

Phase-resolved wave estimation is verified by comparing the mean difference in encounter angle estimates and the correlation for numerical data sets over a one-hour period in long-crested seaways. The time step is set to 10 Hz and the maximal frequency of the PSWF to 1 $\frac{\text{rad}}{\text{s}}$ for the barge and 2 $\frac{\text{rad}}{\text{s}}$ for the small barge. Motion points are distributed along both the longitudinal and transversal axis of the ship.

Fig. 2 presents the mean estimated encounter angles and correlations in various seaways. The values are averaged for the simulated encounter angles ranging from 0° to 180° in 30° increments. Angle estimates are obtained from each time window and the most occuring value for one hour of measurements is chosen. The estimation is calculated using the heave, roll, pitch motion for a speed of 2 $\frac{\text{m}}{\text{s}}$ corresponding to the data listed in Tab. 1. The plots on the left side show the results for the barge and the right side for the small barge. Barge angle estimates show differences in small wave periods, but they diminish as wave periods increase. Small barge angle estimates are comparable, but slightly higher uncertainty is observed for almost all motion points. Correlation values increase with wave period, approaching 1 for both vessels in long waves. Both ships act as low-pass filters at small wave periods, however, the small barge is less sensitive to various motion points. Due to its higher roll eigenfrequency and consequently smaller roll eigenperiod, the small barge exhibits a broader response spectrum. In contrast, the barge response spectrum is dominated by specific frequencies, whereas the small barge's more evenly distributed response is advantageous for PSWF wave profile evaluation.

Fig. 3 shows the same results without averaging of the encounter angles. The top row shows the correlation for $T_\text{p} = 7\,\text{s}$ and the bottom row for $T_\text{p} = 15\,\text{s}$. The figure shows that the correlation in small wave periods for the barge is not reliable enough, but the small barge may be used. It further verifies the low-pass filter behavior of the ships, since the correlation in stern waves is higher than in head waves due to the lower encounter frequencies and therefore higher motion amplitudes. Stern quartering waves strongly reduce the accuracy in low wave periods for the small barge for almost all motion points due to discontinuous RAOs and therefore discontinuous response spectra. Long waves are highly accurate and almost independent of the motion point for the small barge. The barge results show that in beam waves from 90° the correlation decreases for all motion points located on portside or starboard. High rotational motion amplitudes at exposed points are challenging to capture using the inverse problem in Eq. (4). While the rotational transfer functions

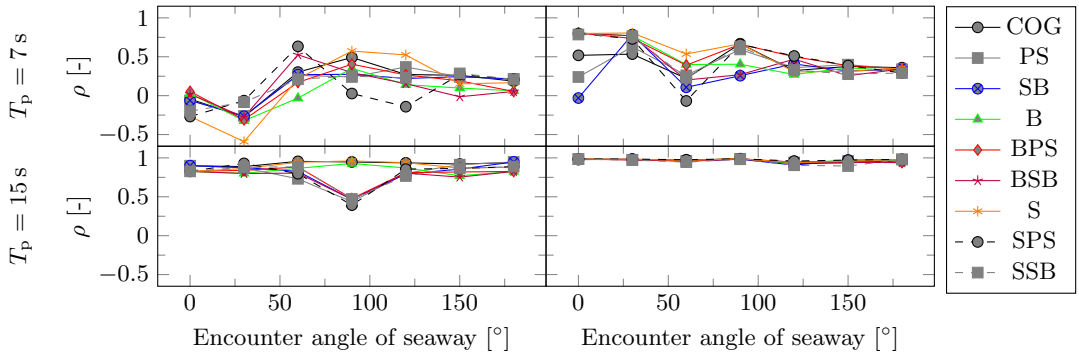

(a) Barge (b) Small Barge

Fig. 3: Comparison of correlation for various motion points along the ship and two peak periods of seaways. Left column displays barge results, right column results for the small barge. Results are shown (COG) indicates the motion point situated at the center of gravity. Additional points are at starboard (SB), portside (PS), stern (S) and bow (B) as well as combinations of the previous points.

remain unchanged, the heave motion transfer function experiences strong amplification for port and starboard points in beam waves due to the rotational terms amplifying the heave motion. The PSWF method relies solely on transfer functions and motion data, limiting the available information. One possible way to improve correlation is by neglecting the rotational terms in Eq. (4). However, this approach has generally led to a further decrease in correlation across all simulations.

4.2 Verification of wave prediction

This section presents the verification of the wave assimilation and prediction algorithm, integrating the developed formulae for the predictable zone of moving ships with numerically generated wave profiles.

Table 2: Wave probe positions used for verification of data assimilation

n_x	n_y	x [m]	y [m]
2	1	0, 100	0
3	2	0, 50, 100	-5, 5
4	3	0, 33.3, 66.6, 100	-15, 0, 15
5	4	0, 25, 50, 75, 100	-15, -5, 5, 15

The probe positions for the following investigations are listed in Tab. 2. In Fig. 4 the coloured subfigures show the correlation for various positions downstream of the point $(0, 0)^T$, which marks the stern of the wave probe array. The probe array is not moving. The seaway is coming from 180° encounter angle and the results are symmetrical along the x-axis. Wave reconstruction is performed using 30 frequencies from five different directions. The results indicate that a high correlation is achieved within a range of approximately 50 m for each configuration. Increasing the number of wave probes enhances accuracy in transversal direction, especially along the second direction next to the main direction. This may be a numerical phenomena, as the seaway itself is generated using five discrete directions.

In Fig. 5 the prediction is performed using an array of 15 probes positioned at $x = [0\,\text{m}, 25\,\text{m}, 50\,\text{m}, 75\,\text{m}, 100\,\text{m}]$ and $y = [-15\,\text{m}, 0\,\text{m}, 15\,\text{m}]$. The probes move at speeds ranging from 0 to 7.5 $\frac{\text{m}}{\text{s}}$. The results show that a higher forward speed has two effects on the resulting scattered correlation. First, overall correlation increases with higher forward speed, as waves need less time to reach the prediction point, reducing information loss. Second, the correlation spread decreases and a clear separation between high and low correlation is forming. The spreading in the prediction zone is generally lower with higher forward speed.

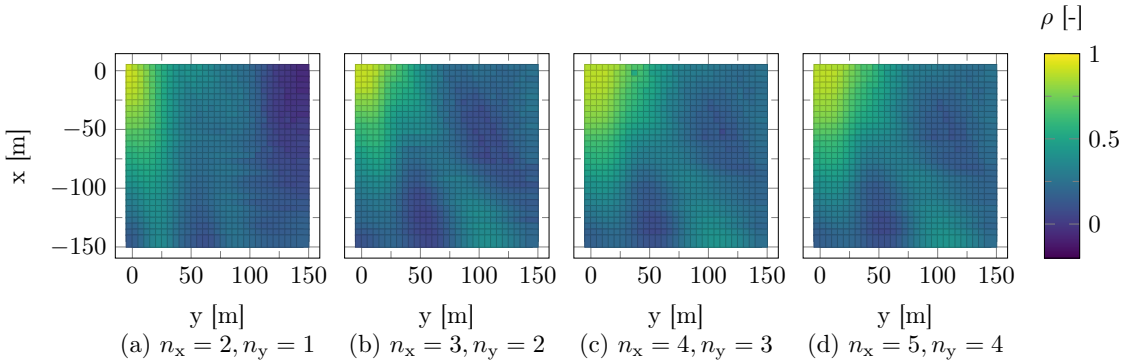

(a) $n_x = 2, n_y = 1$ (b) $n_x = 3, n_y = 2$ (c) $n_x = 4, n_y = 3$ (d) $n_x = 5, n_y = 4$

Fig. 4: Influence of probe array size and probe positions on correlation of wave profiles for the phase resolved wave prediction with numerical input data. Probe array is configured as listed in Tab. 2 and the probes are not moving in a seaway with $\mu = 180°$, $H_s = 2.5\,\text{m}$ and $T_p = 8\,\text{s}$.

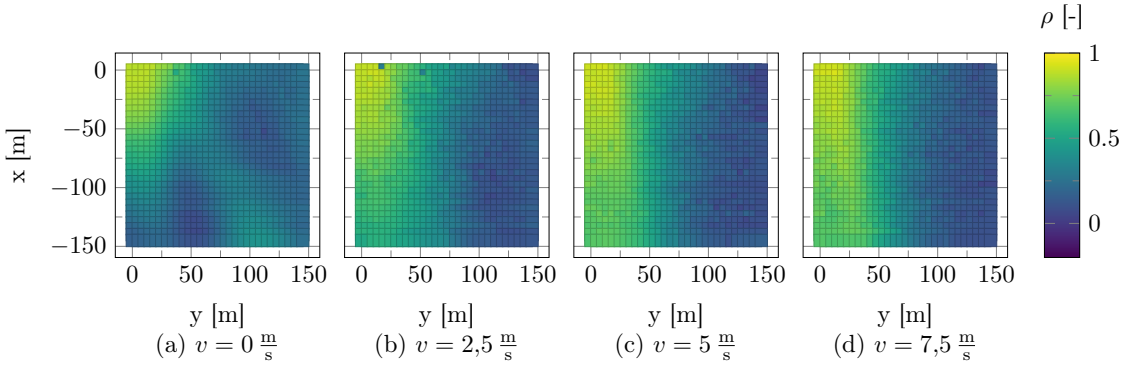

(a) $v = 0\,\frac{\text{m}}{\text{s}}$ (b) $v = 2{,}5\,\frac{\text{m}}{\text{s}}$ (c) $v = 5\,\frac{\text{m}}{\text{s}}$ (d) $v = 7{,}5\,\frac{\text{m}}{\text{s}}$

Fig. 5: Influence of probe speed on correlation of wave profiles for the phase resolved wave prediction with numerical input data. Probes are moving with speeds between $0\,\frac{\text{m}}{\text{s}}$ and $7.5\,\frac{\text{m}}{\text{s}}$ in a seaway with $\mu = 180°$, $H_s = 2.5\,\text{m}$ and $T_p = 8\,\text{s}$.

4.3 Case study verification of combined methodology

Fig. 6 shows the correlation in a seaway with a 120° encounter angle. Results are calculated using the combined methodology for the three case studies. The four columns represent different sea states with increasing wave height and period. In comparison to Fig. 5, the bow quartering waves shift the high-correlation prediction zone accordingly in wave direction. Small sea states result in low wave estimation accuracy and unreliable downstream predictions. The uncertainty between neighbouring prediction points is higher than in the verification of the prediction. It could be reduced with increased simulation time. Differences between case study 1 and case study 2 arise in long waves due to size of the probe array. In case study 2, the upstream barge leads to a greater extent of the probes, enabling a more accurate reconstruction of the short-crested seaway in the prediction zone. Case study 3 achieves the best results, providing the most information in the prediction zone. This is due to the number of observation points and their transverse spacing as well as the independence of the wave estimations of the two small barges.

Fig. 7 shows the possible forecast time $T_{\text{pred}} = T_1 - T$ in wave direction d for the three case studies and sea states. The bottom row additionally shows the correlation, which is the same quantity as in Fig. 6 along the line with an angle of 120°. Prediction times of up to 10 s can be reached, potentially enabling a forecast of two roll periods for the small barge. However, these times are only possible in smaller wave periods with lower phase speeds, which also correspond to lower correlation in the prediction zone. The most practical prediction results occur in case study 3 where one roll period may be forecasted with high correlation and low to medium sea states.

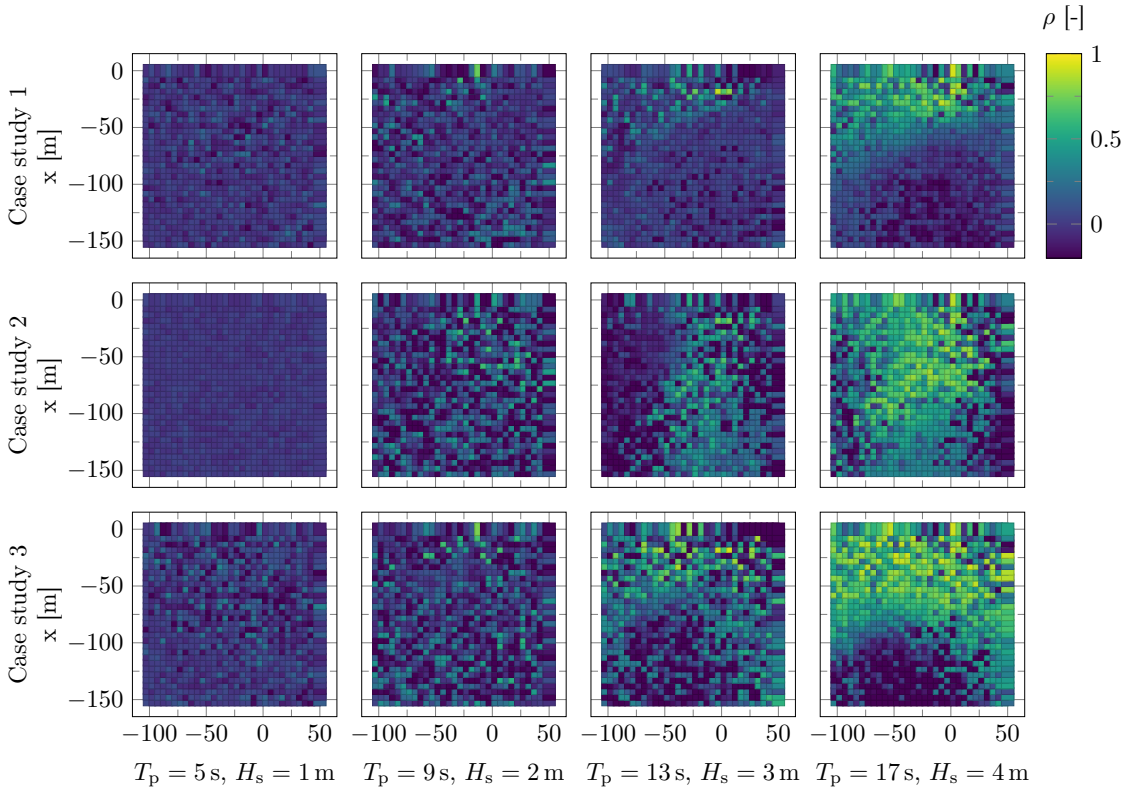

Fig. 6: Correlation of wave profiles predicted with combined methodology in 4 wave conditions and 3 case studies. Ships are moving at a speed of 2 $\frac{m}{s}$ and the waves are coming from 120° encounter angle and the point $\boldsymbol{x} = (0, 0)^T$ indicates the stern of the forward ship or the center of the two small barges in case study 3.

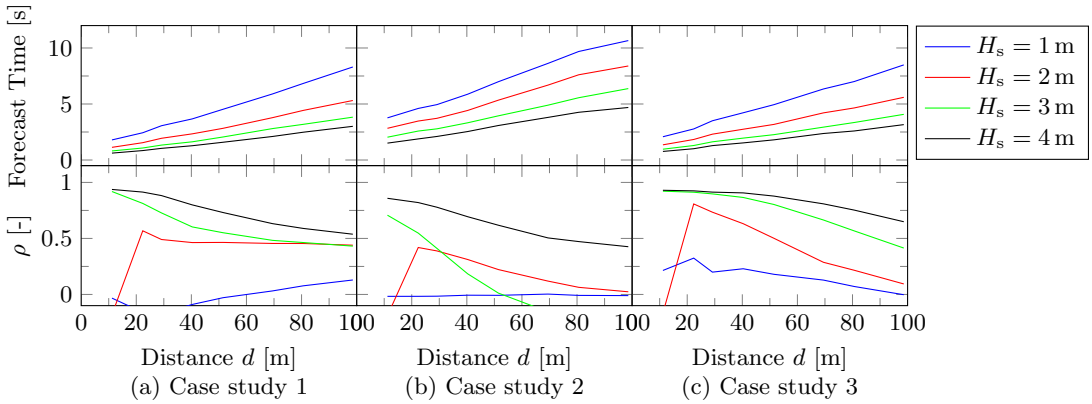

(a) Case study 1 (b) Case study 2 (c) Case study 3

Fig. 7: Possible forecast time according to linear wave theory and correlation of the wave profiles from the 3 case studies. Results are plotted over various distances from the point $\boldsymbol{x} = (0, 0)^T$ in the wave direction of 120° for the 4 wave conditions with wave heights from 1 to 4 m significant wave height and wave periods from 5 to 17 s in steps of 4 s.

5 Conclusion

The combination of wave estimation using Prolate Spheroidal Wave Functions (PSWF) and phase-resolved wave prediction via linear two-dimensional wave assimilation for ships with forward speed, based on motion

measurements, was successfully verified. The methodology was verified against numerical data including 3 case studies of various ship arrangements. Results demonstrate that the accuracy and extent of the downstream prediction zone depend on the wave period and the size of the ship used for estimation. The most accurate predictions were achieved using multiple ship motion measurements from two small barges operating with a lateral distance. However, wave forecasts are limited to time ranges on the order of one roll eigenperiod or less. Future work could explore developments of the PSWF method to increase correlation with small wave amplitudes and assimilation techniques to extend the forecast time, enabling more effective motion prediction.

References

1. Cademartori, G., Oneto, L., Valdenazzi, F., Coraddu, A., Gambino, A., Anguita, D.: A review on ship motions and quiescent periods prediction models. Ocean Engineering **280**, 114822 (Jul 2023). https://doi.org/10.1016/j.oceaneng.2023.114822
2. Chen, J., Hlophe, T., Gunawan, D., Taylor, P.H., Milne, I.A., Zhao, W.: Phase-resolved wave prediction with varying buoy positions in the field using machine learning-based methods. Ocean Engineering **307**, 118107 (Sep 2024). https://doi.org/10.1016/j.oceaneng.2024.118107
3. Hlophe, T., Taylor, P.H., Kurniawan, A., Orszaghova, J., Wolgamot, H.: Phase-resolved wave prediction in highly spread seas using optimised arrays of buoys. Applied Ocean Research **130**, 103435 (Jan 2023). https://doi.org/10.1016/j.apor.2022.103435
4. Johnsen, L., Krüger, S.: Determination of the vertical location of the axis of rotation of the roll motion from full-scale measurements. In: Volume 6: Ocean Engineering. OMAE2021, American Society of Mechanical Engineers (Jun 2021). https://doi.org/10.1115/omae2021-62301
5. Kim, H., Kang, H., Kim, M.H.: Real-time inverse estimation of ocean wave spectra from vessel-motion sensors using adaptive kalman filter. Applied Sciences **9**(14), 2797 (Jul 2019). https://doi.org/10.3390/app9142797
6. Kim, I.C., Ducrozet, G., Bonnefoy, F., Leroy, V., Perignon, Y.: Real-time phase-resolved ocean wave prediction in directional wave fields: Enhanced algorithm and experimental validation. Ocean Engineering **276**, 114212 (May 2023). https://doi.org/10.1016/j.oceaneng.2023.114212
7. Kim, I.C., Ducrozet, G., Leroy, V., Bonnefoy, F., Perignon, Y., Bourguignon, S.: A real-time wave prediction in directional wave fields: Strategies for accurate continuous prediction in time. Ocean Engineering **291**, 116445 (Jan 2024). https://doi.org/10.1016/j.oceaneng.2023.116445
8. Komoriyama, Y., Iijima, K., Tatsumi, A., Fujikubo, M.: Identification of wave profiles encountered by a ship with no forward speed using kalman filter technique and validation by tank tests - long-crested irregular wave case -. Ocean Engineering **271**, 113627 (Mar 2023). https://doi.org/10.1016/j.oceaneng.2023.113627
9. Law, Y., Santo, H., Lim, K., Chan, E.: Deterministic wave prediction for unidirectional sea-states in real-time using artificial neural network. Ocean Engineering **195**, 106722 (Jan 2020). https://doi.org/10.1016/j.oceaneng.2019.106722
10. Liu, Y., Zhang, X., Dong, Q., Chen, G., Li, X.: Phase-resolved wave prediction with linear wave theory and physics-informed neural networks. Applied Energy **355**, 121602 (Feb 2024). https://doi.org/10.1016/j.apenergy.2023.121602
11. el Moctar, B.O., Schellin, T.E., Söding, H.: Numerical Methods for Seakeeping Problems. Springer International Publishing (2021). https://doi.org/10.1007/978-3-030-62561-0
12. Mounet, R.E., Nielsen, U.D., Brodtkorb, A.H., Tannuri, E.A., de Mello, P.C.: Simultaneous sea state estimation and transfer function tuning using a network of dynamically positioned ships. Applied Ocean Research **129**, 103367 (Dec 2022). https://doi.org/10.1016/j.apor.2022.103367
13. Nielsen, U.D.: Transformation of a wave energy spectrum from encounter to absolute domain when observing from an advancing ship. Applied Ocean Research **69**, 160–172 (Dec 2017). https://doi.org/10.1016/j.apor.2017.10.011
14. Qi, Y., Wu, G., Liu, Y., Yue, D.K.: Predictable zone for phase-resolved reconstruction and forecast of irregular waves. Wave Motion **77**, 195–213 (Mar 2018). https://doi.org/10.1016/j.wavemoti.2017.12.001
15. Takami, T., Dam Nielsen, U., Juncher Jensen, J., Maki, A., Matsui, S., Komoriyama, Y.: Onboard identification of stability parameters including nonlinear roll damping via phase-resolved wave estimation using measured ship responses. Mechanical Systems and Signal Processing **210**, 111166 (Mar 2024). https://doi.org/10.1016/j.ymssp.2024.111166
16. Takami, T., Nielsen, U., Jensen, J., Matsui, S.: Nonlinear roll damping identification based on onboard ship response measurements. In: Proceedings of 10th PAAMES and AMEC 2023 (2024), 10th PAAMES / AMEC 2023 ; Conference date: 18-10-2023 Through 20-10-2023

17. Takami, T., Nielsen, U.D., Jensen, J.J., Chen, X.: Estimation of encountered wave elevation sequences based on response measurements in multi-directional seas. Applied Ocean Research **135**, 103570 (Jun 2023). https://doi.org/10.1016/j.apor.2023.103570
18. Takami, T., Nielsen, U.D., Xi, C., Jensen, J.J., Oka, M.: Reconstruction of incident wave profiles based on short-time ship response measurements. Applied Ocean Research **123**, 103183 (Jun 2022). https://doi.org/10.1016/j.apor.2022.103183